The Brittle-Ductile Transition in Porous Limestone: Failure Mode, Constitutive Modeling of Inelastic Deformation and Strain Localization

Patrick Baud, Stephen Hall, Michael Heap, Yuntao Ji, Teng-fong Wong

JGR Solid Earth

RESEARCH ARTICLE
10.1029/2020JB021602

The Brittle-Ductile Transition in Porous Limestone: Failure Mode, Constitutive Modeling of Inelastic Deformation and Strain Localization

Patrick Baud[1], Stephen Hall[2,3], Michael J. Heap[1], Yuntao Ji[4,5], and Teng-fong Wong[6]

[1]Université de Strasbourg, CNRS, Institut Terre et Environnement de Strasbourg, Strasbourg, France, [2]Division of Solid Mechanics, Lund University, Lund, Sweden, [3]Lund Institute of Neutron and X-ray Science, Lund, Sweden, [4]State Key Laboratory of Earthquake Dynamics, Institute of Geology, Beijing, China, [5]HPT Laboratory, Department of Earth Sciences, Utrecht University, Utrecht, The Netherlands, [6]Earth System Science Programme, Faculty of Science, The Chinese University of Hong Kong, Hong Kong

Key Points:

- New triaxial and CT data are presented on Indiana limestone of porosity 16%
- Digital Volume Correlation reveals several complex failure modes involving shear bands through the brittle-ductile transition
- The onset of inelastic compaction in dual porosity allochemical limestones is in agreement with the normality condition

Supporting Information:

Supporting Information may be found in the online version of this article.

Correspondence to:

P. Baud,
patrick.baud@unistra.fr

Citation:

Baud, P., Hall, S., Heap, M. J., Ji, Y., & Wong, T.-f. (2021). The brittle-ductile transition in porous limestone: Failure mode, constitutive modeling of inelastic deformation and strain localization. *Journal of Geophysical Research: Solid Earth*, *126*, e2020JB021602. https://doi.org/10.1029/2020JB021602

Received 22 DEC 2020
Accepted 3 APR 2021

Abstract Understanding of the mechanics of the brittle-ductile transition (BDT) in porous limestone is significantly more challenging than for sandstone because of the lack of consistent acoustic emission activity in limestone, meaning that one must rely on alternative techniques. In this paper, we investigate systematically the failure modes in Indiana limestone using X-ray microComputed Tomography imaging (μCT) and Digital Volume Correlation (DVC). Our new mechanical data show that the envelope for the onset of shear-enhanced compaction can be well approximated by an elliptical cap. The DVC analysis revealed the development of shear bands through the BDT, but no evidence of compaction bands. The shear band angles were between 29° and 46° with respect to the maximum principal stress. Compiling these new results with published data on Purbeck and Leitha limestones, we showed that inelastic compaction in each of these dual porosity allochemical limestones was in a good agreement with the normality condition, as defined in plasticity theory. Comparison of the observed failure modes with predictions based on bifurcation analysis showed that the shear band angles are consistently smaller than the theoretical predictions.

Plain Language Summary A fundamental understanding of the brittle-ductile transition (BDT) in porous sedimentary rocks is important in many geophysical and geological applications. In porous sandstone, a lot of our current understanding of both brittle and ductile behaviors is based on acoustic monitoring. In limestone however, the lack of consistent acoustic emission activity obliges us to rely on alternative techniques. In this paper, we investigated systematically deformation and failure in compression in Indiana limestone using X-ray Computed Tomography imaging, a technique used to image density contrasts. Samples were scanned pre- and post-deformation and image correlation was used to study the various failure modes. Our analysis revealed the development of shear bands through the BDT but no evidence of compaction bands. The shear band angles were between 29° and 46° with respect to the maximum principal stress. Compiling our new results with published data on Purbeck limestone, we showed that inelastic compaction in these allochemical limestones with double porosity (micro- and macro-pores) was in a good agreement with the normality condition, as defined in plasticity theory. Comparison of the observed failure modes with theoretical predictions showed that the shear band angles are consistently smaller than the predicted ones.

1. Introduction

A fundamental understanding of the brittle-ductile transition (BDT) in porous sedimentary rocks is important in geological applications related to reservoir compaction and subsidence (Fisher et al., 1999), borehole stability (Coelho et al., 2005), seismic attenuation (Yarushina & Podladchikov, 2010), earthquake rupture (Andrews, 2007), the stability of volcanic edifices (Bakker et al., 2015; Heap et al., 2013), tectonics of faulting and deformation (Cilona et al., 2012, 2014; Tondi et al., 2006), and fluid flow (Antonellini et al., 2014; Tondi et al., 2016). In this study we focus on the low-temperature BDT, which is associated with primarily cataclastic deformation and manifested by failure modes that depend on mean stress and have little dependence on temperature (Rutter, 1986; Wong & Baud, 2012).

As for other rock types, our basic understanding of the rheology and failure of carbonates derives from experimental rock mechanics. Considering the wide variety of origins and microstructures of carbonates (Folk, 1959), previous experimental studies have investigated several rocks with low (Baud et al., 2000; Fredrich et al., 1989; Rutter, 1974), intermediate (Dautriat et al., 2011; Nicolas et al., 2016; Vajdova et al., 2004), and high (Baxevanis et al., 2006; Baud et al., 2009; Baud, Exner et al.,2017) porosities. A general observation is that the phenomenology of inelastic deformation, failure, and strain localization in porous limestones is similar to that of sandstones, chalks, and tuffs (see Wong & Baud, 2012 for a review). For all these rocks, at relatively low confining pressures, dilatant deformation accompanied by shear localization and brittle faulting are observed, whereas shear-enhanced compaction can develop at higher confinement, which ultimately leads to either delocalized cataclastic flow or compaction band formation.

Beyond phenomenology, a deeper understanding of the mechanics of BDT hinges on addressing several key questions. First, we must identify the stress condition under which a mode of failure can initiate and characterize, in some detail, how the failure mode is manifested in the spatiotemporal evolution of damage. Second, comprehensive mechanical data should be acquired and used to constrain the constitutive model that can realistically capture the inelastic behavior. Third, prediction based on the constitutive model of the mode of failure and how it initiates and develops should be validated with laboratory and microstructural observations.

For porous limestones, several technical challenges need to be tackled before the above questions can be addressed in the laboratory. Unlike crystalline rocks and sandstones, damage in carbonate rocks (associated with dilatant or compactant deformation) results in relatively few acoustic emissions (AE) and, consequently, AE monitoring can provide very limited information on the spatiotemporal development of failure (Schubnel et al., 2006; Vajdova et al., 2004). Furthermore, the spatial clustering of damage in limestones tends to be rather subtle and not readily identified in deformed samples under optical or scanning electron microscopes (Ji et al., 2015). In the past decade, X-ray Computed microTomography (μCT) has emerged as the primary tool for mapping out damage evolution in porous limestones. In a recent study, Huang et al. (2019) demonstrated that synchrotron X-ray μCT can be used to directly image in 4D (3D in space plus time) the multiscale failure and compaction localization in Leitha limestone deformed in triaxial compression. Notwithstanding the efficacy of this in-situ approach, it is not readily implemented in other limestones unless their pore and grain sizes fall within an optimal range. The average grain size and pore dimension should be not too large, probably 1/10 or less of the sample diameter. On the other hand, for the grain-scale deformation processes to be resolvable by μCT imaging the pores cannot be too small and they should have dimensions larger than that of a voxel (several μm in typical μCT studies). This latter constraint handicaps the use of direct μCT imaging for studying damage evolution in many carbonate rocks, especially those with pore spaces made up of not only macropores, but also micropores that are sub-micron in dimension and yet contribute significant fractions towards the total porosity (Bauer et al., 2011; Ji et al., 2012; Lucia, 1995; Zhu et al., 2010).

For rocks with sub-micron fissures and voids, an approach that has proved to be effective for quantifying the damage evolution is the integration of ex-situ imaging of deformed samples with Digital Volume Correlation (DVC) (Buljac et al., 2018). This integrated approach has been applied to sandstones and sands (Charalampidou et al., 2014; Hall et al., 2010; Louis et al., 2006), as well as Majella (Ji et al., 2015) and St. Maximin (Abdallah et al., 2020) limestones with relatively high porosities (30% and 38%). Adopting this approach, the first objective of this study is to integrate ex-situ CT imaging with DVC to characterize the spatial heterogeneity of deformation development associated with failure in Indiana limestone (intermediate porosity of about 16% that includes a significant fraction of microporosity).

Inelastic deformation and failure in granular material (including soil, sandstones, diatomites, and carbonates) is commonly analyzed with a constitutive model based on plasticity theory (Davis & Selvadurai, 2002; Desai & Siriwardane, 1984; Fossum & Fredrich, 2000; Lade & Kim, 1995). Baud et al. (2006) systematically investigated the development of the yield stress and strain hardening of four sandstones, and quantitatively compared the data with predictions from the critical state and cap models (Grueschow & Rudnicki, 2005) that are widely used in geophysical and geotechnical applications. The laboratory data and comparison with the models have furnished useful insights into the applicability and limitation of the constitutive models in relation to sandstones. For porous limestones there is a paucity of data for a similar

comparison with plasticity models, partly due to technical issues with acquiring experimental data to large strains. Accordingly, a second objective of this study is to fill in this data gap, which would then allow us to undertake a systematic comparison of limestone behavior with constitutive models. Our experiments were, thus, conducted on (water-saturated) samples over a sufficiently broad range of effective pressures, with the mode of failure ranging from brittle faulting to distributed cataclastic flow.

Bifurcation analysis allows one to derive critical conditions for the onset of strain localization (Rudnicki & Rice, 1975) with respect to a given constitutive model, which would then provide a theoretical framework for connecting the failure mode transition with constitutive behavior. To analyze this connection, it is necessary to have comprehensive mechanical and microstructural data available, as well as spatial characterization of the deformation that, in our study, is derived from DVC of ex-situ μCT images. As a third objective of this study, we pursued such a bifurcation analysis for Indiana limestone to identify mechanical attributes that influence its failure mode and BDT.

According to bifurcation analysis, the critical condition for the onset of strain localization is sensitive to the constitutive model and, in particular, whether it obeys the normality condition such that the inelastic deformation can be described by an associated flow rule (Bésuelle & Rudnicki, 2004; Issen & Rudnicki, 2000). Baud et al. (2006) concluded that the constitutive behavior of four sandstones was characterized by non-normality, which necessitates the development of a non-associated flow rule and complicates the constitutive modeling. To capture such complexity in sandstones, a recent non-associative model based on the critical state framework (Marinelli & Buscarnera, 2015) has invoked as many as 13 constitutive parameters to describe the inelastic behavior. In contrast, the current study indicates that, unlike most sandstones, the overall behavior of Indiana limestone is in basic agreement with the normality condition. This simplifies the constitutive modeling and opens up the possibility of direct comparison between the experimental data and the analytic results of Rudnicki (2004) on the onset of strain localization and failure mode. Motivated by the new results for Indiana limestone, we extended the analysis in this paper to include two other limestones with dual porosity and assess to what extent the normality condition is also applicable.

2. The Studied Material: Indiana Limestone

The mechanical behavior of Indiana limestone, from the Salem Limestone Formation in the Bedford-Bloomington area of Indiana (USA), has been investigated extensively (Lisabeth & Zhu, 2015; Meng et al., 2019; Myer et al., 1992; Vajdova et al., 2004; Wang et al., 2018; Wawersik & Fairhurst, 1970; Zheng et al., 1989). The Indiana limestone used in these studies, and here, is an allochemical limestone (Folk, 1959), with 65% of its bulk rock volume taken up by allochems (fossil, ooids, and some peloids), and the rest by mostly micritic and sparry cements. The average modal percentages are: calcite 97.1%, magnesite 1.2%, silica 0.8%, alumina 0.7%, iron oxide 0.1%, and undetermined material(s) 0.1% (Indiana Limestone Handbook, ILI, 2007). Furthermore, detailed microstructural observations on intact and deformed samples have been conducted by Vajdova et al. (2012) indicating that Indiana limestone is made up of three very different solid constituents and has grains that are heterogeneous in size, ranging from <5 μm to >300 μm for the micrites and allochems, respectively. The block used here is similar, in terms of composition, grain size, and pore size, to those used in the aforementioned studies.

Based on 2D analysis on thin sections, Zhu et al. (2010) inferred that 68% of the pore space of Indiana limestone comprises micropores with a diameter <33 μm. This partitioning between macroporosity and microporosity is corroborated by mercury injection capillary pressure (MICP) and nuclear magnetic resonance (NMR) relaxation time measurements (Wang et al., 2018), which indicate two populations of pores and pore throats with significant contrast in size. The complexity of pore geometry in 3D was visualized by Ji et al. (2012) using μCT. Segmenting the μCT image of an intact sample into three domains, they identified a domain with gray scale (and porosity) that is intermediate between the solid and void domains (Figure 1). Voxels in this intermediate domain are inferred to have local porosities $<100\%$, presumably corresponding to solid elements embedded with multiple micropores. From their morphological analysis Ji et al. (2012) inferred that, whereas the intermediate domain (embedded with micropores) is percolative, the macropores in Indiana limestone alone do not constitute a connected backbone. This implies that the micropores

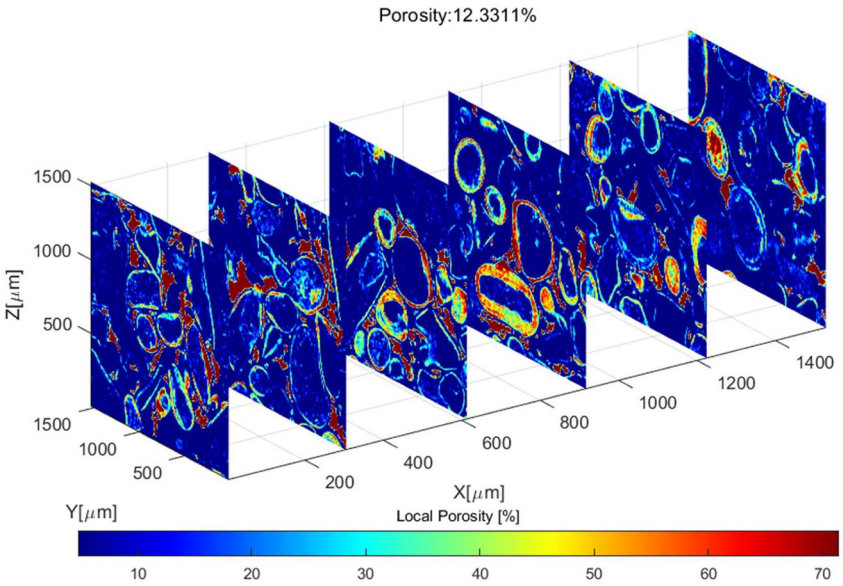

Figure 1. Six slices from a sub-volume of an intact sample of Indiana limestone showing the partitioning between solid grains, macroporosity, and the intermediate zone dominated by microporosity. The μCT data were previously presented by Ji et al. (2012).

likely exert a key role in limiting any fluid circulation, which may explain the relatively low permeability ($<10^{-16}$ m^2) of Indiana limestone as measured at different effective pressures by Wang et al. (2018).

3. Experimental Procedure

3.1. Sample Preparation and Mechanical Deformation

Twelve cylindrical samples with diameter 20 mm were cored perpendicular to the sedimentary bedding. They were then precision ground to a nominal length of 40 mm. The samples were first dried in vacuo at 40°C for a minimum of a week. The bulk density of the samples was then determined from the dry mass and the sample dimensions. We found an average bulk density of 2.28 kg/m^3. Assuming 100% calcite, the corresponding average porosity of our samples was 15.9% ± 0.15%. Porosity measurements were performed on some of these samples using a He pycnometer, and yielded very similar values of porosity.

The samples were oven-dried and then vacuum-saturated with deionized water. Following saturation, the samples were left submersed in deionized water for a minimum of 48 h to ensure chemical equilibrium (Lisabeth & Zhu, 2015). The samples were wrapped in thin (thickness = 0.05 mm) copper foil, jacketed with polyolefine tubing, and then placed inside the conventional triaxial deformation apparatus at the University of Strasbourg (see protocol in Baud et al., 2015). All experiments were performed at ambient laboratory temperature and using a pore fluid pressure of 10 MPa. Fully drained conditions were ensured due to the permeability of the studied Indiana limestone of 3.7×10^{-15} m^2, measured using a benchtop gas (nitrogen) permeameter at the University of Strasbourg (see protocol in Heap et al., 2017). The confining pressure (provided by oil) and pore fluid pressure (deionized water) were controlled by computer-controlled stepping motors connected to pressure transducers with an accuracy of 0.05 MPa. Changes in pore volume, converted to porosity change using the ratio of the pore volume change to the initial bulk sample volume, of a saturated sample was monitored using the displacement of the pore pressure generator using an angular encoder. The error on the pore volume change was 1.0×10^{-12} m^3, which corresponded to an error on the porosity <<1%. The volumetric strain of the sample was also recorded by monitoring the displacement of the confining pressure generator using an angular encoder (see Baud et al. (2009) for more details). The confining and pore fluid pressures were slowly increased to the target pressures and the samples were left under these conditions overnight to ensure microstructural equilibrium. Once equilibrated, an axial load, measured by a load cell, was applied using a steel piston controlled by a third computer-controlled stepping

Table 1
Summary of Mechanical Data for the Samples Investigated in This Study

			Peak stress		Compactive yield stress C*		
Sample	Porosity [%]	Effective pressure [MPa]	*Q* [MPa]	*P* [MPa]	*Q* [MPa]	*P* [MPa]	Comments
IS3	15.8	5	54	23	-	-	DVC: Shear band (29°)
IS1	15.9	10	62.9	31.1	-	-	DVC: Shear bands (29–42°)
IS4	15.8	15	-	-	49	31.3	DVC: Shear bands (42°)
IS12	15.9	15	-	-	49.9	31.7	DVC: Shear bands (37-43-46°)
IS6	16.0	20	-	-	45.1	35.1	DVC: Shear bands
IS8	15.8	30	-	-	40	44.3	DVC: Cataclastic flow
IS5	16.0	40	-	-	35	51.7	Cataclastic flow
IS11	16.0	50	-	-	25.4	58.5	Cataclastic flow
IS2	16.1	*P**	-	-	0	63	Cataclastic flow

Abbreviation: DVC, Digital Volume Correlation.

motor. Axial displacement was monitored using an external linear variable differential transducer (accuracy = 0.2 μm). The piston was programmed to advance at a constant displacement rate corresponding to a constant strain rate of 1.0×10^{-15}/s. The axial load and displacement were converted to axial stress and strain using the sample dimensions.

To acquire mechanical data to constrain the inelastic behavior and for input to constitutive modeling, we performed triaxial deformation tests on eight samples at confining pressures ranging from 15 and 60 MPa. Another sample was hydrostatically compressed to a maximum confining pressure of 140 MPa. The deformation histories of the nine samples are summarized in Table 1.

3.2. X-Ray CT Imaging and Digital Volume Correlation

Six samples (Table 1) were selected for ex-situ μCT imaging. Before and after the triaxial experiments conducted in Strasbourg, the intact and deformed samples were imaged by μCT at the 4D imaging laboratory at Lund University, Sweden, using a Zeiss XRadia Versa XRM 520. All the imaged samples were nominally dry. At the end of each test, the samples were first unloaded to hydrostatic conditions at a strain rate of 10^{-15}/s. The confining and pore pressures were then incrementally reduced to zero and the samples were retrieved from the pressure vessel for ex-situ post-mortem μCT. They then spent a day on a hot plate and were dried in vacuo for 48 h at 40°C.

The μCT data were acquired before and after the triaxial experiments. The pre-deformation scans used an X-ray tube voltage of 90 kV and a power of 8 W with the manufacturer-supplied He1 source filter to reduce beam hardening artifacts. The post deformation scans used an X-ray tube voltage of 110 kV (and a power of 10 W), due to the extra attenuation due to the copper jacket around the sample used in the triaxial tests; this was kept in place to avoid any unnecessary disturbance of the samples. Tomographic reconstruction of the projection data was performed with the Zeiss Xradia Reconstructor software, with minor beam hardening correction to yield 3D image volumes with cubic pixels of 23 μm side length. The gray-scale values of the pre- and post-deformation reconstructed images were scaled to be consistent for the subsequent analysis.

DVC has previously been shown to be effective tool for delineating the geometric complexity of strain localization in porous sandstones (Charalampidou et al., 2011; 2014), limestone (Ji et al., 2015), and andesite (Heap et al., 2020). In this work, the DVC analysis was performed with the open source Python code Spam (Stamati et al., 2020) to the pre- and post-deformation μCT image data for an analysis of the full 3D strain tensor field due to the triaxial deformation.

Local DVC was performed over a regular 3-D grid of nodes distributed over the image in the undeformed state, and a volumetric domain (the "correlation window") centered on each node was used for the correlation analysis. In this study, the grid spacing of the DVC nodes was 20 voxels in each direction and

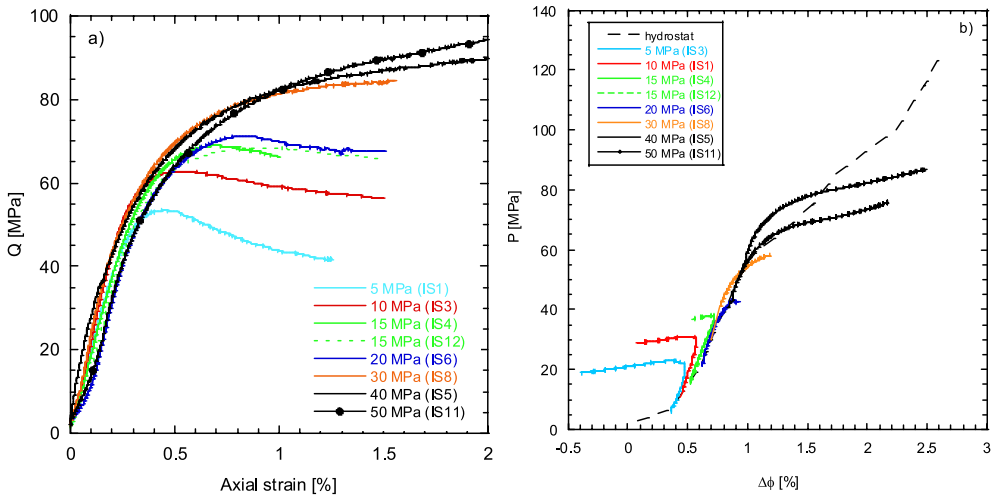

Figure 2. Mechanical data for water-saturated samples of Indiana limestone deformed in conventional triaxial conditions. (a) Differential stress as a function of axial strain. (b) Porosity reduction as a function of effective mean stress. The hydrostat is given for reference.

the correlation window was a cuboid made up of 21 × 21 × 21 voxels centered on the analysis node. The displacement field was derived by identifying the 3-D translation that maximized the cross-correlation of the gray-level data of the undeformed and deformed images within the correlation window at each node. The displacement field so determined is based on a discrete integer unit (related to the voxel dimension), and therefore a further step was used to determine a subvoxel resolved translation vector. This procedure is based on finding the subvoxel-resolved translation that maximizes the correlation between the nodal volume of the undeformed image and an interpolated version of the nodal volume of the deformed image corresponding to the subvoxel translation from the initial, integer translation. Subsequent calculation of the strain tensor is based on the gradient of the displacements over 8-point cubic elements of neighboring nodes. More details can be found in Stamati et al. (2020).

Although we have evaluated all six independent strain components and the principal strain strains ε_1, ε_2, and ε_3 at each node, we will here visualize the spatial distribution of deformation by focusing on two quantities related to the strain tensor invariants: volumetric strain $\varepsilon_v = \varepsilon_1 + \varepsilon_2 + \varepsilon_3$ and a measure of the shear strain $\gamma_s = \sqrt{2\left[\left(\varepsilon_1 - \varepsilon_2\right)^2 + \left(\varepsilon_1 - \varepsilon_3\right)^2 + \left(\varepsilon_2 - \varepsilon_3\right)^2\right]} / 3$, which correspond to first invariant of the strain tensor and $\sqrt{2}$ times the octahedral shear strain (that is also proportional to the square root of the second invariant of the deviatoric strain tensor), respectively.

4. Mechanical Data

We adopt the convention that compressive stresses and compactive strains (i.e., shortening and porosity decrease) are positive. The maximum and minimum principal compressive stresses are denoted by σ_1 and σ_3, respectively. The differential stress Q is defined to be σ_1–σ_3, and the pore pressure is denoted by P_p. The difference between the confining pressure (P_c) and pore pressure will be referred to as the effective pressure P_{eff} and accordingly the difference $P = (\sigma_1+2\sigma_3)/3\text{-}P_p$ between the mean stress and pore pressure will be referred to as the effective mean stress.

The mechanical data for differential stress as a function of axial strain for eight samples of Indiana limestone deformed at different effective pressures (Table 1) are presented in Figure 2a. From 5 to 20 MPa of effective pressure, the differential stress reached a peak beyond which strain softening was observed. At $P_{eff} = 15$ and 20 MPa, we noted that the peak stress was not attained until after a significant axial strain had accumulated. At effective pressures of 30 MPa and higher, the samples strain hardened monotonically up to axial strains of 2%.

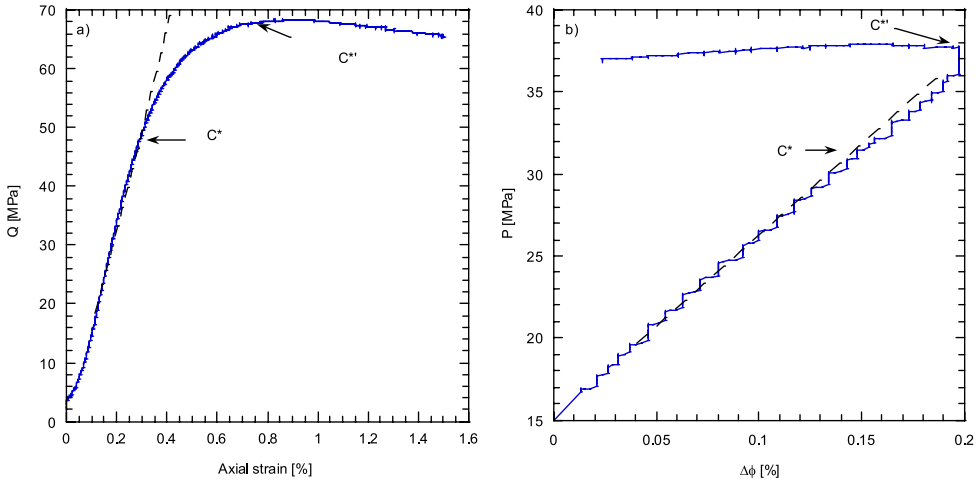

Figure 3. Mechanical data for sample IS12 deformed at an effective pressure of 15 MPa. (a) Differential stress as a function of axial strain. (b) Porosity reduction as a function of effective mean stress. The arrows indicate the critical pressures C^* and $C^{*\prime}$.

Data for the effective mean stress as a function of porosity reduction of the same samples are presented in Figure 2b. We also include for reference the hydrostatic compression curve, with an inflection point $P^* = 63$ MPa that corresponds to the critical pressure at the onset of cataclastic pore collapse (Zhu et al., 2010). At effective pressures of 5 and 10 MPa, appreciable discrepancy with the hydrostat corresponding to the initiation and progressive development of dilatancy was observed in the pre-peak stage, which persisted through the strain softening stage. The stress state at the onset of dilatancy will be denoted by C'. The exterior appearance of the samples indicates shear band formation and brittle faulting. Previous studies of Indiana limestone (Meng et al., 2019; Vajdova et al., 2012) deformed to relatively large strains under similar pressures have reported band angle of ~30°relatively to σ_1. In contrast, at effective pressures of 30 MPa and beyond, shear-enhanced compaction was observed to initiate at effective mean stresses lower than P^*, ranging from 44 to 58 MPa (Figure 2b). The stress state at the onset of shear-enhanced compaction will be denoted by C^*. Judging from the exterior of the deformed samples, localization seems to be absent from this ductile mode of failure at relatively high confinement, in agreement with previous studies (Meng et al., 2019; Vajdova et al, 2004, 2012).

The mechanical data for samples deformed at effective pressures of 15 and 20 MPa indicate a deformation regime that is transitional between brittle faulting and ductile flow. Pre-peak dilatancy was not observed, even though these samples all underwent strain softening and appreciable dilatancy in the post-peak stage. Although the exterior appearance also suggests the absence of strain localization in the two samples (IS4 and IS12) deformed at 15 MPa, the internal development of high-angle shear bands was visualized by DVC, which will be discussed in detail in a later section. What appears to be a tensile crack was observed on the exterior of sample IS6 after deformation, which we interpret to have been induced during unloading. A recent study (Meng et al., 2019) of a water-saturated sample deformed to relatively large strain at effective pressure of 20 MPa reported a band angle of ~45°with respect to σ_1. We highlight the complex interplay of dilatancy and shear-enhanced compaction in this transitional regime by deforming sample IS12 at effective pressure of 15 MPa to a relatively large strain of 1.5% (Figure 3a). The porosity reduction data (Figure 3b) show that shear-enhanced compaction did initiate before reaching the peak stress (at the stress state marked C^*). However, the sample switched to dilatancy at the stress state marked $C^{*'}$ in the near vicinity of the peak stress, which was accompanied by a gradual stress drop. Analogous complexity in the transitional regime has been observed in other porous limestones, including Solnhofen, Tavel, Purbeck, and Majella (from the Orfento formation) limestones (Cilona et al., 2012; Meng et al., 2019; Vajdova et al., 2004).

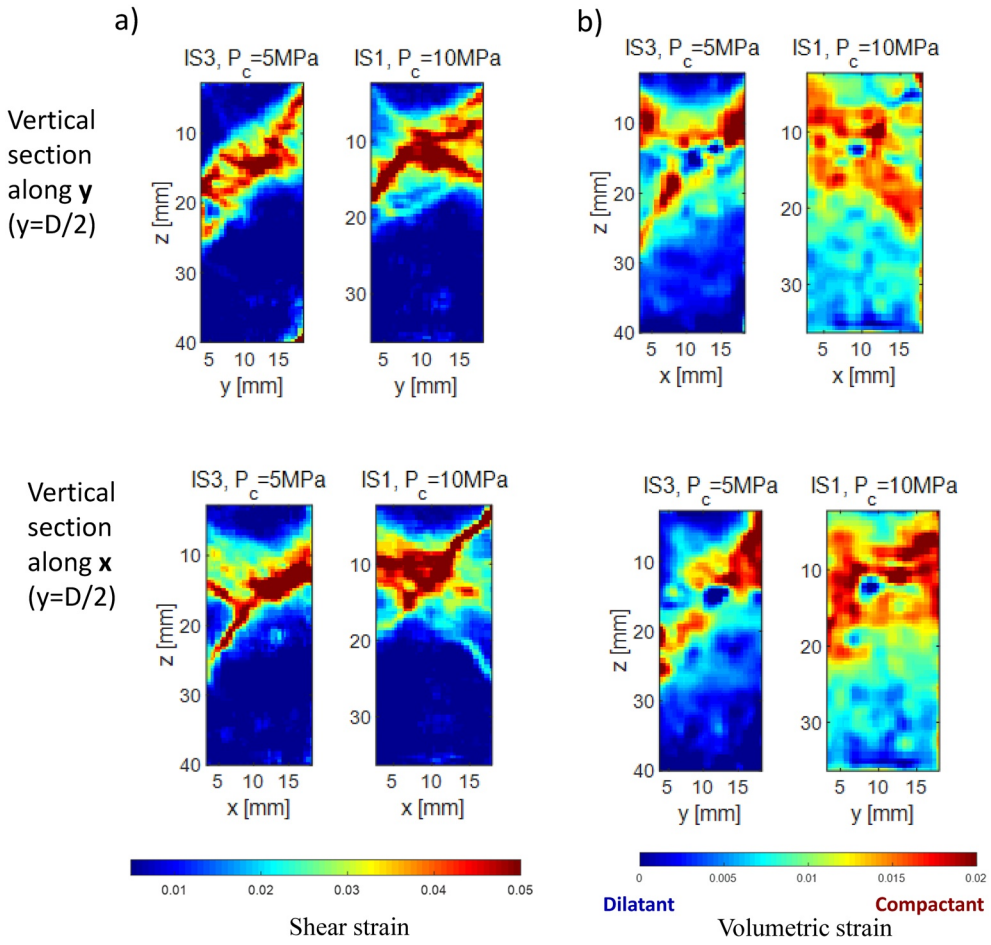

Figure 4. 2D strain distributions on two orthogonal axial planes of two samples of Indiana limestone deformed at 5 and 10 MPa of effective pressures and analyzed by DVC. The shear strain (a) and volumetric strain (b) are presented on the figure. DVC, Digital Volume Correlation.

5. Spatial Distribution and Localization of Strain from Digital Volume Correlation

Six samples (Table 1) were scanned before and after the triaxial compression tests and DVC was performed on each pair of μCT images to evaluate the associated displacement and strain fields. As noted earlier, a tensile crack was visible in the exterior of sample IS6, which we interpreted to be induced by unloading, and corresponding to this a relatively thick extensile zone (located in the lower half of this sample) was also visualized by DVC. Given that the damage in this sample is dominated by artifacts due to unloading and unrelated to the triaxial loading, the DVC data of IS6 will not be included in our presentation here.

The distribution of strains on two orthogonal axial planes are presented in Figure 4 for the two samples IS3 and IS1 deformed at effective pressures of 5 and 10 MPa, respectively. The strain magnitude is on the order of 1%, comparable to the macroscopic strains attained in these mechanical tests. Several angled bands with significant enhancement of shear strain (up to a factor of 5) were visualized (Figure 4a). Given that the volumetric strains are primarily compactive (Figure 4b), these features should probably be categorized as compacting shear bands. Nevertheless, there appear to be localized pockets of dilation, which may have contributed to the dilatancy observed in these two samples in the pre- and post-peak stages.

Synthesis of the 2D strain distributions mapped on orthogonal planes indicates that the shear bands have a geometry that is curved and not exactly planar. Indeed, 3D visualization of the strain concentration (Movies S1 and S2) underscores the geometric complexity of the shear localization, with a network of

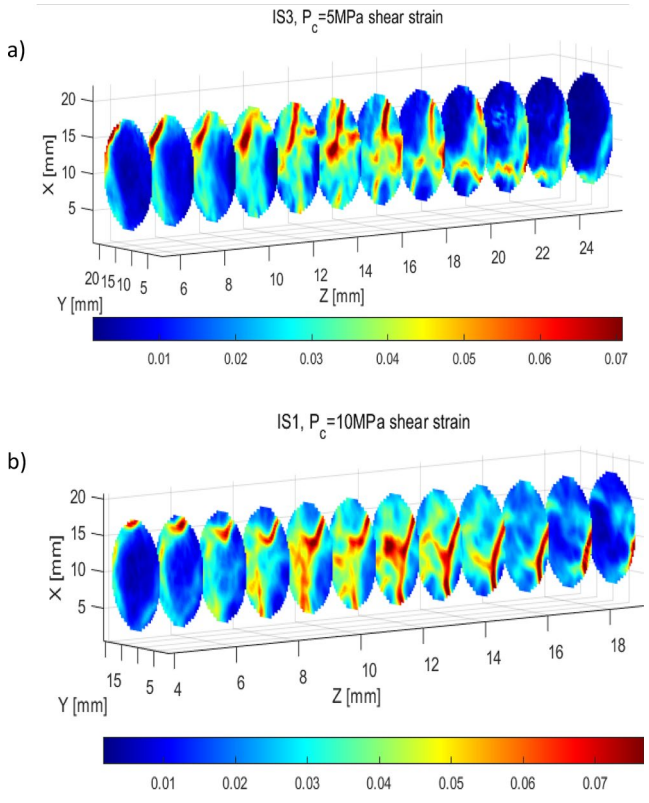

Figure 5. Selected serial sections (with color-coded shear strain) of samples of Indiana limestone IS3 (a) and IS1 (b) deformed at effective pressures of 5 and 10 MPa, respectively. The sections are from planes perpendicular to the sample axis.

intersecting shear bands. The complexity is also highlighted in Figure 5a and Figure 5b with selected serial sections (with color-coded shear strain) on planes perpendicular to the axes of samples IS3 and IS1, respectively. The shear band geometry renders it difficult to unambiguously pinpoint the orientations of the shear bands. However, because we need estimates of the band angle for the latter comparison with prediction of localization theory, we analyzed the images in different perspectives and inferred that IS3 has developed two shear bands both oriented at 29°with respect to σ_1 (Movie S1). We consider that the uncertainty on this orientation and those determined in the following is ±5°. For IS1, it was inferred to have developed two primary shear bands, one oriented at 29° and the other at a higher angle of 42° to σ_1 (Movie S2). Several secondary bands also developed subparallel to the high-angle band.

We next consider the DVC results for samples deformed under higher confinement. In the two samples deformed at effective pressure of 15 MPa (IS4 and IS12), localized zones of shear strain were also visualized (Figure 6), but they have geometric attributes somewhat different from the two samples IS1 and IS3 in the brittle faulting regime, as indicated by 3D visualization of the strain concentration (Movies S3 and S4) which has developed in shear zones that seem to be more diffuse and at higher angles. This is highlighted in selected serial sections on planes perpendicular to the axes of samples IS4 and IS12, respectively (Figures 7a and 7b). We also inferred that IS4 developed two conjugate shear bands both oriented at an angle of 42° with respect to σ_1, and IS12 a primary shear band oriented at 43°. Several incipient conjugate bands have also developed at angles ranging from 37° to 46°.

6. Discussion

By integrating *ex-situ* μCT imaging with DVC, we have identified the transition of failure mode with effective pressure in Indiana limestone and delineated the 3D distribution of strain in relation to failure mode. We have also acquired comprehensive mechanical data which allows us to next constrain the constitutive model with reference to the inelastic behavior. The constitutive model so calibrated will be adopted in a bifurcation analysis to predict the mode of failure and its development, which are then compared with our laboratory and microstructural observations.

6.1. Elliptical Yield Cap and Constitutive Modeling

Our deformation experiments were conducted on limestone samples saturated with deionized water, which is expected to undergo ionic exchange with the solid grains when initially introduced into the pore space, until the increase in calcite concentration renders the saturation state of the fluid and the rock to be in equilibrium. Experimental observation and modeling have indicated that equilibrium would require ~50 h at 25°C (Lisabeth & Zhu, 2015), which has guided our sample preparation. That a stable microstructure can be so attained is supported by the reproducibility of the data of Wang et al. (2018) and Meng et al. (2019) for effective stress coefficients of several limestones over several loading and unloading cycles.

The presence of water may lower somewhat the strength of a limestone in both the brittle and ductile fields, in comparison with a nominally dry sample (Baud et al., 2016; Baud, Exner et al., 2017; Baud, Schubnel et al., 2017; Nicolas et al., 2016). For the latter, the strains are commonly measured by strain gages, which are limited to relatively small strain and sensitive to any developments of heterogeneity or localization (Baud et al., 2000; Vajdova et al., 2004). In contrast, the use of porosimetry allows for a robust measurement of the global strains in a sample deformed to large strains. We expect the overall behavior in water-saturated and nominally dry samples to be qualitatively similar, as illustrated by a comparison of our data to those

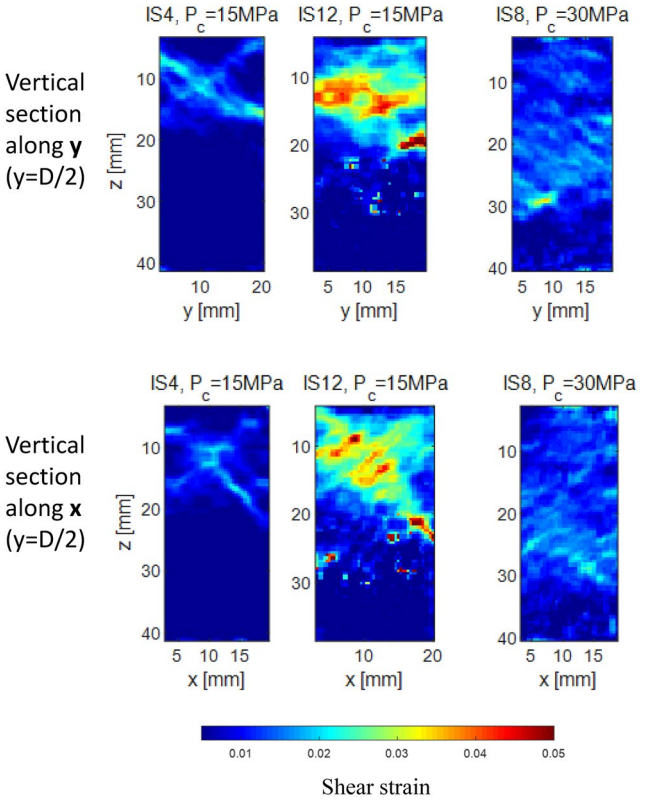

Figure 6. 2D strain distributions on three orthogonal axial planes of three samples of Indiana limestone deformed at 15 (IS4 and IS12) and 30 MPa (IS8) of effective pressures and analyzed by DVC. The shear strain is presented on the figures. DVC, Digital Volume Correlation.

of Vajdova et al. (2004) (Figure 8). Vajdova et al. (2004) studied nominally dry samples of Indiana limestone with porosities comparable to ours, and their data for the brittle strength, the critical stress C^* for onset of shear-enhanced compaction, and the critical stress $C^{*'}$ for the transition from compaction to dilation are comparable to our corresponding data for water-saturated samples, following similar trends with respect to increase of effective mean stress P.

To highlight the fundamental differences in compactive yield behavior between porous limestones and sandstones, we plot in Figure 9a the C^* data for dry Solnhofen, Tavel and Indiana limestones (Baud et al., 2000; Vajdova et al., 2004) with porosities ranging from 3% to 16% and compare them with water-saturated Bentheim sandstone (Baud et al., 2006) with a porosity of 23%. The four sets of C^* data have the common attribute in that they can be approximated as caps with an elliptical shape, but there is a fundamental difference in location of the yield stresses on the caps. For each of the limestones, shear-enhanced compaction was observed only in stress states lying on the right side of the ellipse, with a negative slope. Our data for water-saturated Indiana limestone (Figure 8) follow the same trend. In contrast, shear-enhanced compaction in Bentheim sandstone was observed not only on the right, but also on the left side of the ellipse, which has a positive slope. As discussed in the next section, if the normality condition applies, then a positive slope would necessarily imply dilatancy and since compaction was instead observed, the implication is that the behavior of Bentheim sandstone violates normality and one must resort to a non-associative flow rule to describe its constitutive behavior. Baud et al. (2006) observed that this non-associative flow behavior is common to the four sandstones that they investigated.

Following Baud et al. (2006), data for the onset of shear-enhanced compaction were fitted with an elliptic yield cap in P-Q space, with semi-axes A and B and center at C:

$$\frac{(P-C)^2}{A^2}+\frac{Q^2}{B^2}=1 \tag{1}$$

The cap for our Indiana limestone C^* data has values of $A = 30$ MPa, $B = 50$ MPa, and $C = 30$ MPa. As shown in Figure 9b, the yield stresses attained after a porosity reduction of 1% also fall on an ellipse with larger semi-axes. For reference, we also plotted the stress states C' of samples IS1 and IS3 at the onset of dilatancy, which fall on the left side of the cap with a positive slope.

Noting that P corresponds to the first stress invariant I_1 and Q is related to the second deviatoric stress invariant J_2 ($=\left[(\sigma_{11}-\sigma_{22})^2+(\sigma_{22}-\sigma_{33})^2+(\sigma_{33}-\sigma_{11})^2\right]/6+\sigma_{12}^2+\sigma_{23}^2+\sigma_{31}^2$) of the stress tensor σ_{ij} in axisymmetric compression, the elliptic yield cap can alternatively be expressed as a yield function in the following form (Baud et al., 2006):

$$f(\sigma_{ij})=\frac{(I_1-c)^2}{a^2}+\frac{J_2}{b^2}-1=0 \tag{2}$$

The coefficients in Equations 1 and 2 are related by: $A = a/3$, $B=\sqrt{3}b$, and $C = c/3$.

Rudnicki (2004) have derived detailed results for an elliptic yield cap, which guide our latter discussion of experimental data and comparison with model prediction. However, a slight difference in notation should be noted: whereas his coefficients a and c are identical to our A and C in Equation 1, his b is identical to our b in Equation 2.

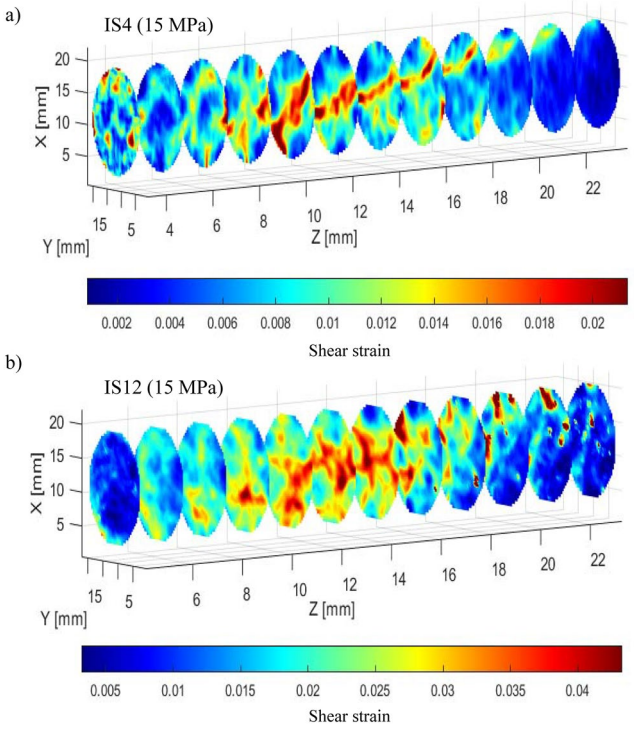

Figure 7. Selected serial sections (with color-coded shear strain) of samples of Indiana limestone IS4 (a) and IS12 (b) both deformed at an effective pressure of 15 MPa. The sections are from planes perpendicular to the sample axis.

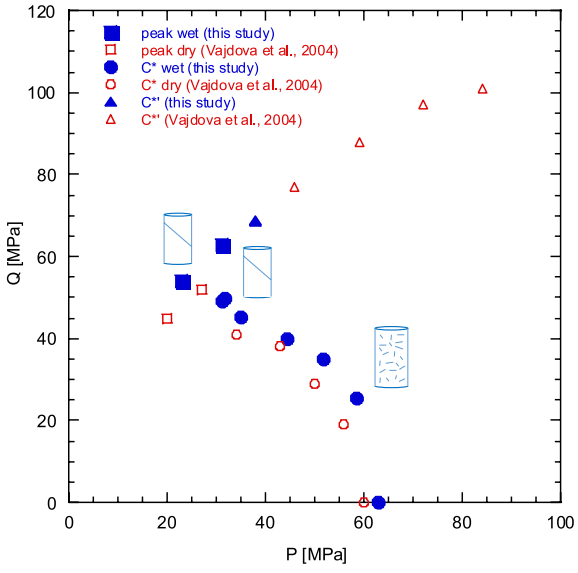

Figure 8. Stress states C', C*, C*' and peak stress are shown in the stress space for water-saturated Indiana limestone (blue symbols). The data of Vajdova et al. (2004) on dry Indiana limestone are also presented as red symbols.

6.2. Normality Condition and Associated Flow Rule

In plasticity theory, the normality condition follows from Drucker's (1951) postulate of material stability, which prescribes an "associated flow rule" for the plastic increment $\Delta\varepsilon_{ij}^{p}$ of the strain tensor ε_{ij} in term of the derivative of the yield function f with respect to the stress σ_{ij}:

$$\Delta\varepsilon_{ij}^{p} = \frac{\partial f}{\partial \sigma_{ij}}\Delta\lambda \tag{3}$$

Since $\Delta\lambda$ is a positive scalar, the associated flow rule implies that the plastic strain increment is orthogonal to the yield surface, which represents a condition of normality (Davis & Selvadurai, 2002; Desai & Siriwardane, 1984).

Because a conventional triaxial test is axisymmetric, the strain tensor of an isotropic rock can be characterized by the two independent measurements of axial and volumetric strain. Combining the yield function (Equation 2) with the normality condition (Equation 3), we derive the ratio between the volumetric and axial components of the plastic strain as:

$$\frac{\Delta\varepsilon_{ii}^{p}}{\Delta\varepsilon_{11}^{p}} = \frac{18b^{2}\left(I_{1}-c\right)}{a^{2}\left(2\sigma_{11}-\sigma_{22}-\sigma_{33}\right)+6b^{2}\left(I_{1}-c\right)} \tag{4a}$$

Denoting the volumetric component by $\Delta\varepsilon_{v}^{p} = \Delta\varepsilon_{ii}^{p}$ and axial component by $\Delta\varepsilon^{p} = \Delta\varepsilon_{11}^{p}$ and connecting the principal stresses to the stress quantities P an Q, the above reduces to (Baud et al., 2006):

$$\frac{\Delta\varepsilon_{v}^{p}}{\Delta\varepsilon^{p}} = \frac{3}{\left(3A^{2}\,/\,B^{2}\right)\left(Q\,/\left(P-C\right)\right)+1} \tag{4b}$$

This allows one to evaluate the plastic strain ratio at a point (P,Q) that lies on the yield cap. Using the parameter values for A, B, and C of Indiana limestone (30, 50, and 30 MPa, respectively), the ratio $\Delta\varepsilon_{v}^{p}\,/\,\Delta\varepsilon^{p}$ was evaluated as a function of $P_{eff} = P - Q\,/\,3$ at the onset of shear-enhanced compaction (Figure 10). According to the associated flow rule (Equation 4b), the plastic strain ratio decreases from a maximum value of 3 under hydrostatic loading at $P_{eff} = P^{*}$ to very negative values at low pressures. The ratio undergoes a transition from positive to negative at the peak of the cap, given by $(P,Q) = (C,B)$ that is attained by triaxial compression at the effective pressure $P_{eff}^{BDT} = C - B\,/\,3$, with a value of 13.3 MPa in water-saturated Indiana limestone (Figure 9b).

To assess whether the accumulation of plastic strain obeys normality, we analyzed the mechanical data (Figure 2) following the approach of Wong et al. (1997). In a porous rock with relatively stiff solid grains, the plastic component of volumetric strain derives primarily from the plastic component of porosity change $\Delta\Phi^{p}$, which implies that $\Delta\varepsilon_{v}^{p} \approx \Delta\Phi^{p}$. In the laboratory we have measured the total increment of porosity change (induced by an increment of axial strain) which, after appropriate subtraction of the elastic components, can be used to evaluate the plastic components $\Delta\Phi^{p}$ and $\Delta\varepsilon^{p}$. The ratio $\Delta\Phi^{p}\,/\,\Delta\varepsilon^{p}$ corresponds to the "inelastic compaction factor" (Wong et al., 1997), which we evaluated from the mechanical data and compared with prediction of (Equation 4b). Indeed,

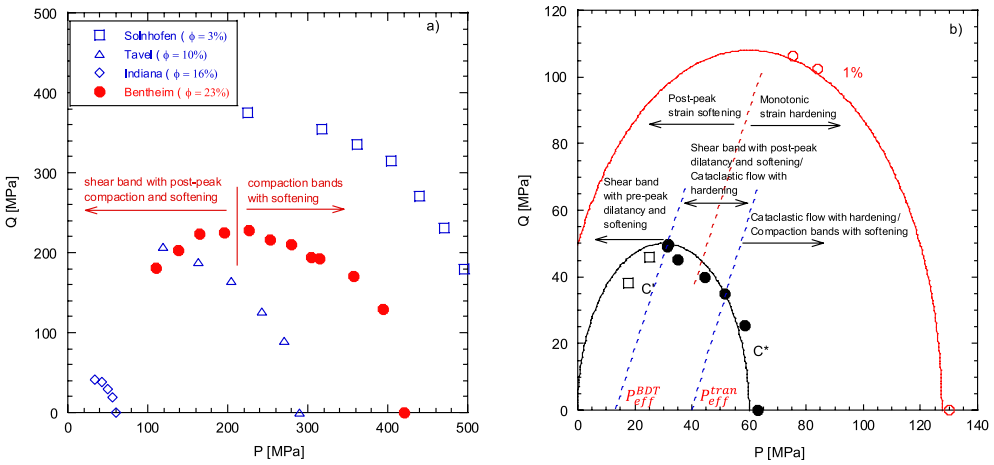

Figure 9. (a) Comparison in the stress space between the envelopes for the onset of shear-enhanced compaction C* for wet Bentheim sandstone (red circles, Baud et al., 2006) and wet Indiana limestone (blue diamonds). For reference, the data dry Tavel (blue triangles) and dry Solnhofen limestones (blue squares) of Vajdova et al. (2004) are also presented on the graph. For Bentheim sandstone the transition between the domains for shear bands with post-peak compaction and softening and compaction bands with softening is shown. (b) Initial yield stress C* (black circles) and its evolution for a plastic volumetric strain of 1% (red open circles) for Indiana limestone. The experimental data were fitted with elliptical caps. The aspect ratio (B/A) of the yield cap was 1.7. For reference the data for the onset of dilatancy C′ are shown as open back squares. The stress paths for P_{eff}^{BDT} and P_{eff}^{tran} (Equation 6) and the transition from softening and hardening are also shown, as blue and red dashed line, respectively.

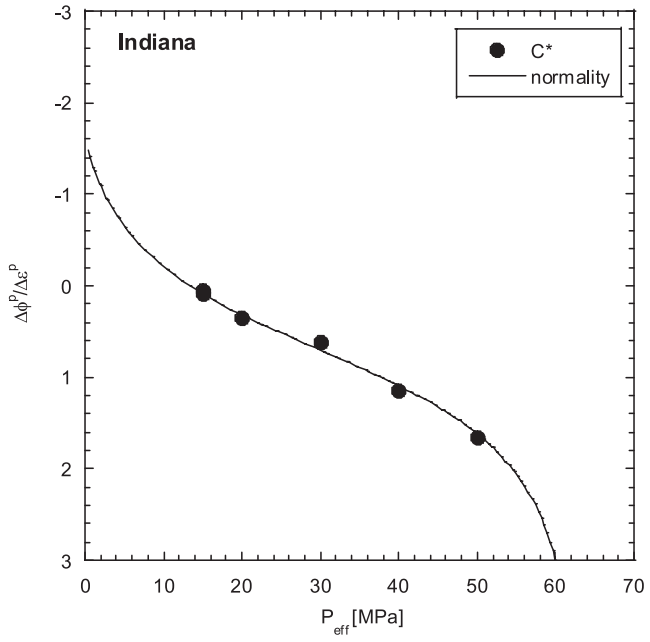

Figure 10. Comparison of experimental data with prediction of the normality condition in Indiana limestone. The inelastic compaction factor at the onset of shear-enhanced compaction C* as a function of the effective pressure at which a triaxial compression experiments was conducted. Solid line represents the theoretical predictions for associative behavior according to Equation 4b.

the inelastic compaction factors inferred so from data show reasonable agreement with prediction of the associated flow rule (Figure 10), with the implication that Drucker's postulate of material stability and normality is applicable to Indiana limestone.

This agreement with the normality condition motivates us to further test the postulate with two other limestones, which have recently been investigated in relation to the BDT and permeability evolution (Baud, Exner, et al., 2017; Brantut et al., 2018; Meng et al., 2019). The Purbeck limestone from England is made up of calcitic peloids (100–500 μm) in the form of micrites surrounded by sparry cement, as well as polycrystalline quartz dispersed in the aggregate. The porosity of Purbeck limestone is 13.8% and the pore space is made up of macropores and significant fraction of micropores (Wang et al., 2018). The Leitha limestone from Austria is a grainstone made up of cemented bioclasts of relatively uniform size. Due to changes in the depositional regime, the porosity, cementation, and pore structure of Leitha limestones are highly variable. Based on their detailed microstructural analysis, Baud, Exner, et al. (2017) concluded that the limestone pore space can be categorized into two end members. In one end member, the pore space has significant proportions of both macropores and micropores. Samples of Leitha limestone (with porosity of 18%) associated with this end member with dual porosity will be analyzed here. In the other end member, the pore space is dominated by macropores, with negligible microporosity. Such a Leitha limestone was used in the study of Huang et al. (2019).

We will use here the data obtained by Brantut et al. (2014) and unpublished data from the study of Baud, Exner, et al. (2017) on water-saturated samples of Purbeck and Leitha limestones, respectively. The mechanical tests were performed over a wide range of effective pressures through the

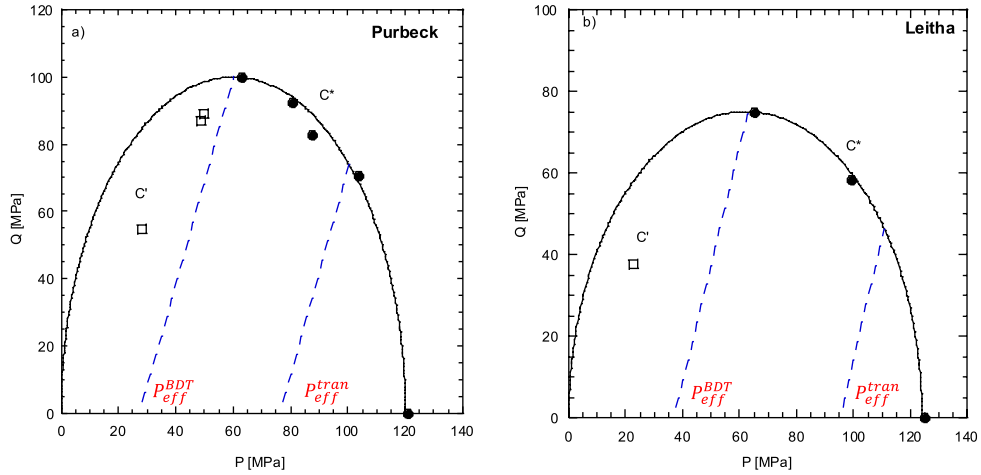

Figure 11. Initial yield stress C* (black circles) for (a) Purbeck limestone (Brantut et al., 2014) and (b) Leitha limestone. The experimental data were fitted with an elliptical cap with aspect ratio (B/A) of 1.7 for Purbeck and 1.21 for Leitha. For reference the data for the onset of dilatancy C' are shown as open back squares. The stress paths for P_{eff}^{BDT} and P_{eff}^{tran} (Equation 6) are also shown, as blue dashed lines.

BDT, in the same conditions than those on Indiana limestone presented in section 3.1. The critical pressure P^* was found to be 121 and 125 MPa for Purbeck and Leitha limestones, respectively.

The elliptic caps that fit the C^* data for water-saturated Purbeck (Figure 11a) and Leitha (Figure 11b) limestones have parameter values of $(A,B,C) = (60,100,60)$ and $(62,75,62)$ in units of MPa, respectively. For Purbeck limestone, we also plotted the stress states C' of two samples that ultimately failed by brittle faulting at effective pressures of 10 and 20 MPa. Both points fall on the left side of the cap with a positive slope, and the effective pressure that corresponds to the peak of the cap is $P_{eff}^{BDT} = 26.7$ MPa (Figure 11a). For Leitha limestone, the data are limited, with two samples on the right side of the cap that showed shear-enhanced compaction, and one that failed by dilatant faulting on the left side. The effective pressure that corresponds to the peak of the cap is $P_{eff}^{BDT} = 37.0$ MPa.

Following the procedure of Wong et al. (1997) we estimated the inelastic compaction factor $\Delta\Phi^p / \Delta\varepsilon^p$ from experimental data for four samples of Purbeck limestone (Figure 12a) and two samples of Leitha limestone (Figure 12b). Again, the compaction factors inferred from experimental data are in good agreement with the prediction according to the associated flow rule (Equation 4b), which corroborates the validity of the normality condition in a another two limestones with dual porosity.

6.3. Failure Mode Transition in Two Limestones with Dual Porosity

With reference to the plasticity model, we will next investigate the onset of strain localization and failure mode using Rudnicki and Rice's (1975) bifurcation analysis for a dilatant frictional material that is characterized by three constitutive parameters (together with two elastic moduli): an internal friction parameter μ, a dilatancy factor β, and a hardening modulus h. It is an isotropic hardening model that allows for nonnormality in the yield behavior if μ and β have different values. However, if the plastic flow is associative, then the equality $\beta = \mu$ would simplify the localization analysis.

Wong et al. (1997) have shown that the dilatancy factor is related to the inelastic compaction factor inferred from the experimental data of a triaxial test:

$$\beta = -\sqrt{3}\frac{\Delta\Phi^p / \Delta\varepsilon^p}{\left(3 - \Delta\Phi^p / \Delta\varepsilon^p\right)} \tag{5a}$$

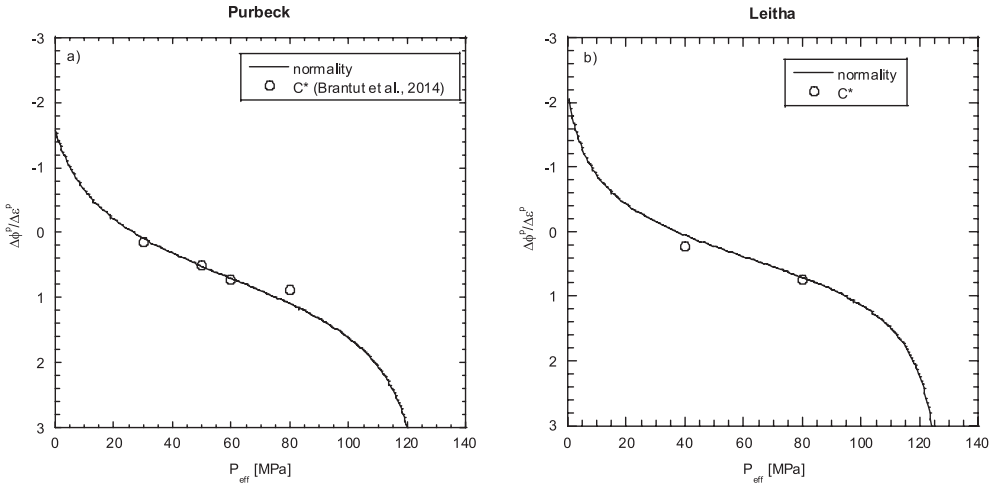

Figure 12. Comparison of experimental data with prediction of the normality condition in (a) Purbeck and (b) Leitha limestone. The inelastic compaction factor at the onset of shear-enhanced compaction C* as a function of the effective pressure at which a triaxial compression experiments was conducted. Solid line represents the theoretical predictions for associative behavior according to Equation 4b.

As for the parameter μ it corresponds to the local slope of the yield envelope in P-Q space multiplied by a factor of $\sqrt{3}/3$, which for the elliptic cap (Equation 1) is given by (Baud et al., 2006):

$$\mu = -\frac{B^2(P-C)}{\sqrt{3}A^2Q} \tag{5b}$$

The critical conditions for the inception of strain localization associated with various failure modes can then be derived by a bifurcation analysis (Issen & Rudnicki, 2000; Rudnicki & Rice, 1975). A transition in failure mode is predicted to occur at critical values of the constitutive parameters, as summarized in Figure 13 for an axisymmetrically compressed rock that satisfies the normality condition. With an increase in confinement, inelastic behavior of the rock undergoes a transition from dilatant to compactant, manifested by a progressive decrease of the constitutive parameters β and μ from being positive to negative. The Rudnicki & Rice (1975) model predicts that a transition in failure mode would occur if the trade-off between the dilatancy and frictional parameters is such that $\beta + \mu = -\sqrt{3}$, which simplifies to $\mu = -\sqrt{3}/2$ for associative flow. On one hand, if $\mu \geq -\sqrt{3}/2$ then shear bands would develop if the rock undergoes strain softening at a sufficiently negative slope. It should be noted that shear bands are predicted to develop not only for yield stresses that lie on the left side of the cap (with a positive μ), but also for part of the right side (with a negative $\mu \geq -\sqrt{3}/2$). On the other hand, if $\mu < -\sqrt{3}/2$ then strain localization in the form of compaction bands may develop, with the necessary condition that the rock attains a peak stress and undergoes strain softening at a sufficiently negative slope. However, if the rock strain hardens in a monotonic manner, then plastic flow is predicted to develop instead in a delocalized manner, independent of whether the friction parameter μ is greater than or smaller than the critical value $-\sqrt{3}/2$.

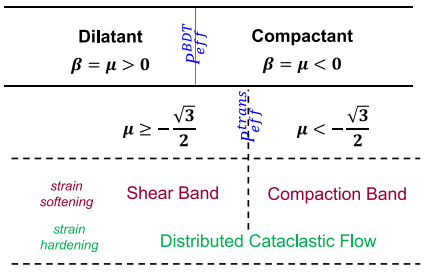

Figure 13. Diagram summarizing the different failure modes as a function of the constitutive parameters.

Following Rudnicki (2004) we will refer to the critical effective pressure for this transition in failure mode as P_{eff}^{tran} (Figure 13). For an elliptic cap (with aspect ratio $\alpha = B/A$) we can substitute (Equation 5b) into the condition $\mu = -\sqrt{3}/2$ to obtain $2\alpha^2(P-C) = 3Q$, which together with Equation 1 for the cap implies that $(P-C) = A/\sqrt{1+(4/9)\alpha^2}$ and $3Q = 2\alpha^2 A/\sqrt{1+(4/9)\alpha^2}$ for the stress state (P,Q) on the cap that

is associated with the transition in failure mode. For comparison with experimental data, it is more convenient to directly relate to the effective pressure, and noting that $P_{eff} = P - Q/3$ and $P^* = A + C$ the critical effective pressure for the transition is derived as:

$$P_{eff}^{tran} = P^* - A\left(1 - \frac{1 - (2/9)\alpha^2}{\sqrt{1 + (4/9)\alpha^2}}\right) \tag{6}$$

Corresponding to the yield cap parameters of Indiana limestone, this transition pressure is inferred to be 40.7 MPa. The loading paths for triaxial compression under the two critical pressures P_{eff}^{BDT} and P_{eff}^{tran} are shown as dashed lines in Figure 9b. At effective pressures lower than P_{eff}^{BDT} the samples (IS1, IS3) developed dilatancy before attaining a peak stress, after which they strain softened and failed by shear localization. At effective pressures greater than P_{eff}^{tran}, samples IS5 and IS11 strain hardened monotonically and failed by distributed cataclastic flow. Although the theory predicts that the samples deformed at high pressure may alternatively develop compaction bands, this failure mode requires the rock to strain soften, which the preexisting pore structure and stress-induced damage seem to inhibit in this limestone with dual porosity. In the transition regime with $P_{eff}^{BDT} \le P_{eff} \le P_{eff}^{tran}$, whether shear bands would develop or not again hinges on the hardening behavior. In samples IS4, IS12 and IS6 strain softening and dilatancy were observed after the critical stress $C^{*'}$ was attained in the vicinity of the peak stress, and shear bands developed. In contrast, sample IS8 strain hardened monotonically and did not develop shear localization.

Data and failure modes for the other two limestones show similar agreement with the bifurcation analysis. In the brittle faulting regime, two samples of Purbeck limestone (Figure 11a) and one sample of Leitha limestone (Figure 11b) deformed at effective pressures lower than P_{eff}^{BDT} failed by shear faulting accompanied by softening, with dilatancy that initiated in the pre-peak stage. In the ductile regime, a broad spectrum of failure mode was observed in Purbeck limestone. At effective pressures above $P_{eff}^{tran} = 76.4$ MPa, the sample deformed at 80 MPa failed by distributed cataclastic flow with strain hardening. In the transitional regime $P_{eff}^{BDT} \le P_{eff} \le P_{eff}^{tran}$, whereas three samples (deformed at effective pressures of 30, 40, and 50 MPa) failed with dilatancy and softening in the post-peak stage, one sample deformed at 70 MPa failed by cataclastic flow with strain hardening. For Leitha limestone, there are only two samples deformed in the transition regime $P_{eff}^{BDT} \le P_{eff} \le P_{eff}^{tran} = 95.6$ MPa: one sample (deformed at effective pressure of 40 MPa) failed with dilatancy and post-peak softening, and the other (deformed at effective pressure of 80 MPa) failed by cataclastic flow with strain hardening.

Our analysis of the inelastic and failure behavior of Indiana, Leitha and Purbeck limestones show that they share several common features. The yielding behavior in each can be described by plastic flow associated with an elliptic cap. The failure mode and its transition with effective pressure are in basic agreement with bifurcation analysis. According to the analysis, compaction band formation would be a viable failure mode only if the limestones show strain softening at high effective pressures. However, in both limestones monotonic strain hardening was observed, which would therefore inhibit the potential development of compaction bands.

The pore spaces of the three limestones also share the common feature that they comprise macropores and significant fractions of micropores. Zhu et al. (2010) observed that in such a limestone with dual porosity, the key micromechanical process of pore collapse does not initiate simultaneously in pores of all sizes, but instead nucleates from only larger pores assisted by damage development in multiplicity of micropores that surround the macropores. Such a "cataclastic pore collapse" process has been observed in several limestones with dual porosity (Vajdova et al., 2010, 2012). Whereas the simultaneous collapse of pores of all sizes may readily result in coalescence and strain softening, it is plausible that the preferential failure of only the larger pores would render the cataclastic pore collapse to be a micromechanical process that promotes hardening, thus inhibiting the development of compaction bands in a porous limestone with dual porosity. One may speculate that, in a limestone not associated with such a duality in its pore space, compaction banding is less inhibited and more ready to occur. Indeed, the contrast in failure mode observed in the two end members of Leitha limestone seems to corroborate this: In the end member with its pore space dominated by mac-

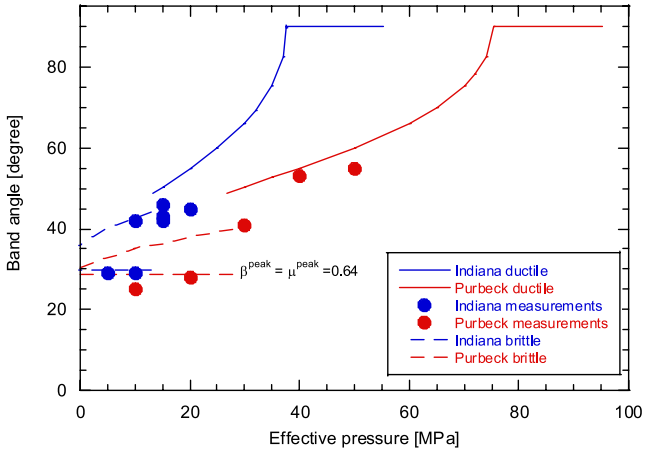

Figure 14. Comparison of the band angles in deformed samples with the theoretical predictions. Band angles with respect to the major principal stress are plotted as a function of the effective pressure. The band angles observed in Indiana and Purbeck limestones are shown as blue and red circles, respectively. For the brittle regime, theoretical predictions based on Equation 8a 8b are shown as blue and red dotted lines for Indiana and Tavel limestone, respectively. For the ductile regime, the predictions of Equation 7a are shown as plain blue and red lines, for Indiana and Purbeck limestone, respectively.

ropores, the progressive development of five discrete compaction bands was documented *in situ* by synchrotron CT imaging (Huang et al., 2019), in contrast to the delocalized cataclastic flow documented for the other end member with dual porosity (Baud, Exner, et al., 2017; this study). Our analysis of the mechanical data for the former end member has shown that the inelastic deformation violates normality and must be described by a non-associative flow rule.

The micromechanics of inelasticity in the end member of Leitha limestone with predominately macropores is similar to porous sandstones, in that the damage primarily derives from pore collapse and grain crushing, mechanisms that may involve frictional dissipation. Indeed, plastic flow behavior in most porous sandstones is also non-associative (Baud et al., 2006). Using an internal variable framework, Rice (1975) has shown that normality in macroscopic plasticity would result from a microstructural arrangement that depends on the stress state only through the thermodynamically conjugate force, but since a frictional mechanism involves the coupled effect of the resolved shear and normal stresses, one cannot readily identify the force that is conjugate to the microstructural arrangement related to pore collapse and grain crushing, with the implication that non-associative flow behavior is generally expected in these sandstones and limestones. However, our data here for three limestones with dual porosity are consistent with plastic normality, even though the microscale deformation mechanisms are similar. A key difference that comes to mind is that, as noted earlier the microstructural arrangement in these three limestones involves the complex interplay of micropores and macropores that occurs at multiple scales. To what extent Rice's (1975) internal variable framework is directly applicable here, and how the analysis can be generalized to microscale deformation mechanisms at multiple scales are important questions that warrant further and deeper investigation.

6.4. Angle of Shear Band

If a shear band were to develop, the bifurcation analysis can be used to predict its orientation. We will denote by θ the angle between the strike of the shear band and the direction of σ_1. As elaborated in Appendix 1, in the transitional regime $P_{eff}^{BDT} \le P_{eff} \le P_{eff}^{tran}$ an upper bound on the shear band angle is given by:

$$\theta = \frac{\pi}{4} + \frac{1}{2}\sin^{-1}\left[1 - \frac{2(1+\nu)}{3}(1-\rho)\right] \tag{7a}$$

$$\rho = \frac{2\alpha^2}{9}\left(\frac{1 - 9S^2/\alpha^2}{1 - S\sqrt{1 + 9(1-S^2)/\alpha^2}}\right), \tag{7b}$$

where ν denotes Poisson's ratio and the dimensionless parameter $S = (P_{eff} - C)/A$. This upper bound is plotted in Figure 14 as solid lines for Indiana and Purbeck limestones at effective pressures greater than P_{eff}^{BDT}, assuming a Poisson's ratio of 0.3 for both. The angle is predicted to increase from a minimum of 49° at P_{eff}^{BDT} to maximum of 90° at P_{eff}^{tran}. For comparison we plot the shear band angles evaluated from the DVC analysis and exterior measurements on our failed samples (Table 1). Indeed, our measured shear band angles are consistently lower than corresponding angles predicted by Equation 7a, with the two Purbeck

samples deformed at effective pressures of 40 and 50 MPa showing angles quite close to the bound. A similar analysis was not conducted for Leitha limestone because of limited data.

We next consider brittle faulting at effective pressures below P_{eff}^{BDT}. In this regime the failure envelope is typically linear (Figure 8), corresponding to Coulomb failure with an almost constant μ^{peak}. We show in Appendix 1 that an upper bound for the band angle can also be obtained as:

$$\theta = \frac{\pi}{4} + \frac{1}{2}\sin^{-1}\left[1 - \frac{2(1+\nu)}{3}\left(1 - \frac{\rho}{2} + \frac{\mu^{peak}}{\sqrt{3}}\right)\right], \tag{8a}$$

We also propose in Appendix 1 an alternative approximation based on the normality condition at the peak stress, which implies that the shear band angle is then given by:

$$\theta = \frac{\pi}{4} + \frac{1}{2}\sin^{-1}\left[1 - \frac{2(1+\nu)}{3}\left(1 + \frac{2\,\mu^{peak}}{\sqrt{3}}\right)\right], \tag{8b}$$

The shear band angles according to (Equations 8a and 8b) are plotted as dotted lines in Figure 14 at effective pressures less than P_{eff}^{BDT}, with $\mu^{peak} = 0.64$ as inferred from the Coulomb failure envelopes of the two limestones. Whereas the upper bound (Equation 8a) is predicted to increase with increasing effective pressure, the approximation (Equation 8b) predicts a constant value of $\theta = 29.9°$. The fault angles (Table 1) observed in all four samples in the brittle faulting regime actually fall very close to this constant value. As expected, they are all below the upper bound (Equation 8a), but interestingly the samples that failed at effective pressures just above P_{eff}^{BDT} have shear band angles that are close to the prediction of (Equation 8a).

In addition to the band angle, the bifurcation analysis also predicts the critical stiffness below which a shear or compaction band may develop. For shear band formation at a pressure $P_{eff} \le P_{eff}^{tran}$, if we again assume an elliptic cap and normality, then the critical stiffness normalized by the shear modulus G is given by (Rudnicki, 2004):

$$\frac{k_{cr}}{G} = -\frac{2(1-\nu)}{9}(1-\rho)^2 \tag{9}$$

Using parameters for the initial yield caps of Indiana and Purbeck limestones, the above would imply values of k_{cr}/G ranging from −0.29 to −0.10, corresponding to a softening slope that is steeper than what we observed in the laboratory data by orders of magnitude. This inability of Rudnicki and Rice's (1975) model to quantitatively predict the critical stiffness for the onset of strain localization has also been observed in Carrara marble (Fredrich et al., 1989) and Berea sandstone (Bernabé & Brace, 1990). To circumvent this limitation, it has been proposed that additional features should be incorporated into the constitutive model, including a corner on the yield envelope and stress-induced anisotropy (Rudnicki, 1977, 2002).

Two limitations should be noted in such a comparison of laboratory data with theoretical predictions of band angle and critical stiffness. First, strictly speaking the bifurcation results here are for the onset of strain localization under a remotely applied stress field, whereas a laboratory sample is subject to boundary effects, as manifested by the geometric complexity of localization and curvature of shear bands revealed by DVC here (Figures 5 and 6). Second, as shown in the recent in-situ synchrotron CT study of Huang et al. (2019), bifurcations in the form of discrete compaction bands in Leitha limestone were associated with abrupt stress drops (presumably with very steep softening slopes in better agreement with bifurcation analysis), which could only be detected by a high-frequency recording system. This raises the possibility that, in our samples that show overall softening with relatively gentle slopes (Figure 2), the initiation of shear bands could have been triggered by episodic stress drops that occurred abruptly and were not detected. Though somewhat speculative, this possibility should be investigated in a future study by acquiring and scrutinizing mechanical data at higher acquisition frequencies.

7. Conclusion

With this paper, we presented new mechanical data on water-saturated Indiana limestone, an allochemical carbonate with a dual porosity (macro- and micro-pores). Using μCT and DVC, we were able to map out the spatial distribution of damage in samples deformed close to and within the BDT. Our new results revealed in particular the development of strain localization beyond the BDT up to an effective pressure of 20 MPa. While complex failure modes involving shear bands were observed, no compaction band could be detected by DVC in Indiana limestone, in agreement with previous studies. We compiled our new results on Indiana limestone with data on Purbeck and Leitha limestones (Baud, Exner, et al., 2017; Brantut et al., 2014), two other limestones with a dual porosity, and showed that for these three rocks the envelope for the onset of shear-enhanced compaction could be approximated by an elliptical cap. Phenomenologically, inelastic compaction in these limestones was therefore similar to previous observations on porous sandstones (Wong & Baud, 2012). We compared the data on Indiana and Purbeck limestone with theoretical predictions based on plasticity theory and showed in all cases a good agreement between the data and the normality condition. In this sense, the results on limestones with dual porosity presented here differ significantly from the previous data on several porous sandstones analyzed by Baud et al. (2006). Future work should be performed to check whether the normality conditions would hold for other porous carbonates. Bifurcation analysis also provides predictions for the orientation of the shear-bands. We observed some discrepancies between the predictions of the model of Rudnicki (2004) and our observations. Our analysis suggested that *in-situ* μCT imaging on Indiana limestone could potentially clarify the reasons behind the differences between the theory and the experiments.

Appendix 1: Localization Analysis and Shear Band Angle

The bifurcation analysis predicts that the angle between the strike of the shear band and the direction of σ_1 is given by (Issen & Rudnicki, 2000; Rudnicki, 2004):

$$\theta = \frac{\pi}{4} + \frac{1}{2}\sin^{-1}\left[1 - \frac{2(1+\nu)}{3}\left(1 + \frac{\beta+\mu}{\sqrt{3}}\right)\right] \tag{A1}$$

Here ν denotes Poisson's ratio, and we next follow Rudnicki (2004) to introduce an angle ϕ such that $\sqrt{3}\tan\phi = Q/(P-C)$ for a stress state (P,Q) that lies on the elliptic cap, and a dimensionless parameter $S = (P_{eff} - C)/A$ to relate the corresponding effective pressure to the center C and semi-axis A of the cap. The two parameters are connected according to Rudnicki's equation (19): $\tan\phi = \sqrt{3}\left(1 - S\sqrt{1 + 9(1-S^2)/\alpha^2}\right)/\left(1 - 9S^2/\alpha^2\right)$. For the elliptic cap the frictional parameter μ is given by (Equation 5b) above, which in Rudnicki's (2004) notation reduces to $3\mu = -\alpha^2/\tan\phi$ and

$$\mu = -\frac{\alpha^2}{3\sqrt{3}}\left(\frac{1 - 9S^2/\alpha^2}{1 - S\sqrt{1 + 9(1-S^2)/\alpha^2}}\right) \tag{A2}$$

If we first focus on the elliptic cap for initial yield and assume that the normality condition $\mu^* = \beta^*$ is valid, then substituting (A2) into (A1) will give:

$$\theta = \frac{\pi}{4} + \frac{1}{2}\sin^{-1}\left[1 - \frac{2(1+\nu)}{3}(1-\rho)\right] \tag{A3}$$

$$\rho = -\frac{2\mu^*}{\sqrt{3}} = \frac{2\alpha^2}{9}\left(\frac{1 - 9S^2/\alpha^2}{1 - S\sqrt{1 + 9(1-S^2)/\alpha^2}}\right) \tag{A4}$$

The asterisk is used to indicate that a constitutive parameter is associated with initial yield C^*. Because shear localization typically occurs near the peak stress, where the constitutive parameters may attain different values $\left(\mu^{peak}, \beta^{peak}\right)$ and the flow may also become non-associative ($\mu^{peak} \neq \beta^{peak}$), the expression above which is based on associative flow with constitutive parameter at initial yield may not be valid near the peak stress. In the transitional regime, as the sample strain hardens to attain the stress state $C^{*'}$, the elliptic cap expands with shear-enhanced compaction, maintaining an almost self-similar geometry (Figure 9b), which suggests that the corresponding slopes are comparable and therefore $\mu^{peak} \approx \mu^*$ at the stress states C* and $C^{*'}$. However, although the rate of compaction seems almost constant during the initial stage of shear-enhanced compaction, it switches to dilatancy in the vicinity of $C^{*'}$ and peak stress (Figure 3), which implies that the relevant β^{peak} should be positive and quite different from the negative $\beta^* = \mu^*$ associated with initial yielding at C^*. From (A1) it can be seen that a higher dilatancy factor results in a smaller angle, and accordingly the angle θ inferred from (Equation 7a) assuming normality and initial yield should be considered as an upper bound.

We next consider brittle faulting at effective pressures below P_{eff}^{BDT}. In this regime the failure envelope is typically linear (Figure 8), corresponding to Coulomb failure with an almost constant slope and μ^{peak}. In this case dilatancy typically initiates at the stress C', evolves with an almost constant rate, and then undergoes drastic increase in the vicinity of the peak stress. At the initiation stage, the dilatancy factor β^* can be evaluated assuming normality (Figures 10 and 12) using (A2) associated with the initial yield cap at C' (Figures 9 and 11). Knowing that dilatancy accelerates near the peak stress and therefore $\beta^{peak} > \beta^* = \mu^*$, using this estimate of β^* in equation (A1) will therefore provide an upper bound for the band angle:

$$\theta = \frac{\pi}{4} + \frac{1}{2}\sin^{-1}\left[1 - \frac{2\left(1+\nu\right)}{3}\left(1 + \frac{\beta^* + \mu^{peak}}{\sqrt{3}}\right)\right] = \frac{\pi}{4} + \frac{1}{2}\sin^{-1}\left[1 - \frac{2\left(1+\nu\right)}{3}\left(1 - \frac{\rho}{2} + \frac{\mu^{peak}}{\sqrt{3}}\right)\right] \quad \text{(A5)}$$

Because dilatancy accelerates near the peak stress, it is difficult to pinpoint from laboratory data the dilatancy factor β^{peak}. To provide an estimate, if we assume the normality condition is valid at the peak stress so that we have the equality $\beta^{peak} = \mu^{peak}$, then (A1) implies that the band angle can be evaluated as:

$$\theta = \frac{\pi}{4} + \frac{1}{2}\sin^{-1}\left[1 - \frac{2\left(1+\nu\right)}{3}\left(1 + \frac{2\,\mu^{peak}}{\sqrt{3}}\right)\right] \quad \text{(A6)}$$

Data Availability Statement

The data are available to the scientific community at https://doi.org/10.6084/m9.figshare.14317313.v1

Acknowledgments
The authors have benefitted from discussions over the years with John Rudnicki on strain localization. The authors thank Fanbao Meng for preparing the 3D visualization in the supplementary materials. The authors are grateful to John Rudnicki and an anonymous reviewer, as well as the editors for their constructive comments and suggestions. This study was partially supported by funding from the Hong Kong Research Grants Council GRF14323916, the France-Hong Kong Collaborative Program Procore 30805PM and F-CUHK405/16, CNRS (PICS 07961). This study was also partially funded by LabEx Grant ANR-11-LABX-0050_G-EAU-THERMIE-PROFONDE (this research therefore benefited from state funding managed by the Agence National de la Recherche (ANR) as part ofthe "Investissements d'avenir" program).

References

Abdallah, Y., Sulem, J., Bornet, M., Ghabezloo, S., & Stefanou, I. (2020). Compaction banding in high porosity carbonate rocks: 1. Experimental observations. *126*, e2020JB020538. *Journal of Geophysical Research: Solid Earth*. https://doi.org/10.1029/2020JB020538

Andrews, D. J. (2007). Compaction can limit peak vertical velocity at Yucca Mountain. *Eos, Transactions American Geophysical Union*, *88*(52). .

Antonellini, M., Cilona, A., Tondi, E., Zambrano, M., & Agosta, F. (2014). Fluid flow numerical experiments of faulted porous carbonates, Northwest Sicily (Italy). *Marine and Petroleum Geology*, *55*, 186–201. https://doi.org/10.1016/j.marpetgeo.2013.12.003

Bakker, R. R., Violay, M. E. S., Benson, P. M., & Vinciguerra, S. C. (2015). Ductile flow in sub-volcanic carbonate basement as the main control for edifice stability: New experimental insights. *Earth and Planetary Science Letters*, *430*, 533–541. https://doi.org/10.1016/j.epsl.2015.08.017

Baud, P., Exner, U., Lommatzsch, M., Reuschlé, T., & Wong, T.-f. (2017a). Mechanical behavior, failure mode, and transport properties in a porous carbonate. *Journal of Geophysical Research: Solid Earth*, *122*(9), 7363–7387. https://doi.org/10.1002/2017jb014060

Baud, P., Reuschlé, T., Ji, Y., Cheung, C. S. N., & Wong, T. f. (2015). Mechanical compaction and strain localization in Bleurswiller sandstone. *Journal of Geophysical Research: Solid Earth*, *120*, 6501–6522. https://doi.org/10.1002/2015JB012192

Baud, P., Rolland, A., Heap, M., Xu, T., Nicolé, M., Ferrand, T., et al. (2016). Impact of stylolites on the mechanical strength of limestone. *Tectonophysics*, *690*, 4–20. https://doi.org/10.1016/j.tecto.2016.03.004

Baud, P., Schubnel, A., Heap, M., & Rolland, A. (2017). Inelastic compaction in high-porosity limestone monitored using acoustic emissions. *Journal of Geophysical Research: Solid Earth*, *122*, 9989–10010. https://doi.org/10.1002/2017jb014627

Baud, P., Schubnel, A., & Wong, T.-f. (2000). Dilatancy, compaction, and failure mode in Solnhofen limestone. *Journal of Geophysical Research*, *105*, 19289–19303. https://doi.org/10.1029/2000jb900133

Baud, P., Vajdova, V., & Wong, T.-f. (2006). Shear-enhanced compaction and strain localization: Inelastic deformation and constitutive modeling of four porous sandstones. *Journal of Geophysical Research*, *111*, B12401. https://doi.org/10.1029/2005JB004101

Baud, P., Vinciguerra, S., David, C., Cavallo, A., Walker, E., & Reuschlé, T. (2009). Compaction and failure in high porosity carbonates: Mechanical data and microstructural observations. *Pure and Applied Geophysics*, *166*, 869–898. https://doi.org/10.1007/978-3-0346-0122-1_7

Bauer, D., Youssef, S., Han, M., Bekri, S., Rosenberg, E., Fleury, M., & Vizika, O. (2011). From microcomputed tomography images to resistivity index calculations of heterogeneous carbonates using a dual-porosity pore-network approach: Influence of percolation on the electrical transport properties. *Physical Review E*, *84*, 011133. https://doi.org/10.1103/physreve.84.011133

Baxevanis, T., Papamichos, E., Flornes, O., & Larsen, I. (2006). Compaction bands and induced permeability reduction in Tuffeau de Maastricht calcarenite. *Acta Geotech.*, *1*, 123–135. https://doi.org/10.1007/s11440-006-0011-y

Bernabé, Y., & Brace, W. F. (1990). Deformation and fracture of Berea sandstone. *American Geophysical Union Geophysical Monograph*, *56*, 91–101. https://doi.org/10.1029/gm056p0091

Bésuelle, P., & Rudnicki, J. W. (2004). Localization: Shear bands and compaction bands. In Y. Guéguen, & M. Boutéca (Eds.), *Mechanics of fluid-saturated rocks* (pp. 219–321). Amsterdam: Elsevier Academic Press.

Brantut, N., Baker, M., Hansen, L. N., & Baud, P. (2018). Microstructural control of physical properties during deformation of porous limestone. *Journal of Geophysical Research: Solid Earth*, *123*(6), 4751–4764. https://doi.org/10.1029/2018jb015636

Brantut, N., Heap, M. J., Baud, P., & Meredith, P. G. (2014). Mechanisms of time-dependent deformation in porous limestone. *Journal of Geophysical Research: Solid Earth*, *119*(7), 5444–5463. https://doi.org/10.1002/2014jb011186

Buljac, A., Jailin, C., Mendoza, A., Neggers, J., Taillandier-Thomas, T., Bouterf, A., et al. (2018). Digital volume correlation: Review of progress and challenges. *Experimental Mechanics*, *58*, 661–708. https://doi.org/10.1007/s11340-018-0390-7

Charalampidou, E.-M., Hall, S. A., Stanchits, S., Lewis, H., & Viggiani, G. (2011). Characterization of shear and compaction bands in a porous sandstone deformed under triaxial compression. *Tectonophysics*, *503*, 8–17. https://doi.org/10.1016/j.tecto.2010.09.032

Charalampidou, E.-M., Hall, S. A., Stanchits, S., Viggiani, G., & Lewis, H. (2014). Shear-enhanced compaction band identification at the laboratory scale using acoustic and full-field methods. *International Journal of Rock Mechanics and Mining Sciences*, *67*, 240–252. https://doi.org/10.1016/j.ijrmms.2013.05.006

Cilona, A., Baud, P., Tondi, E., Agosta, F., Vinciguerra, S., Rustichelli, A., & Spiers, C. J. (2012). Deformation bands in porous carbonate grainstones: Field and laboratory observations. *Journal of Structural Geology*, *45*, 137–157. https://doi.org/10.1016/j.jsg.2012.04.012

Cilona, A., Faulkner, D. R., Tondi, E., Agosta, F., Mancini, L., Rustichelli, A., et al. (2014). The effects of rock heterogeneity on compaction localization in porous carbonates. *Journal of Structural Geology*, *67*, 75–93. https://doi.org/10.1016/j.jsg.2014.07.008

Coelho, L. C., Soares, A. C., Ebecken, N. F. F., Alves, J. L. D., & Landau, L. (2005). The impact of constitutive modeling of porous rocks on 2-D wellbore stability analysis. *Journal of Petroleum Science and Engineering*, *46*, 81–100. https://doi.org/10.1016/j.petrol.2004.08.004

Dautriat, J., Bornert, M., Gland, N., Dimanov, A., & Raphanel, J. (2011). Localized deformation induced by heterogeneities in porous carbonate analysed by multi-scale digital image correlation. *Tectonophysics*, *503*(1–2), 100–116. https://doi.org/10.1016/j.tecto.2010.09.025

Davis, R. O., & Selvadurai, A. P. S. (2002). *Plasticity and geomechanics*. Cambridge University Press.

Desai, C. S., & Siriwardane, H. J. (1984). Constitutive laws for engineering materials, with emphasis on geologic materials, 19. Prentice Hall.

Drucker, D. C. (1951). A more fundamental approach to plastic stress strain relations. *Proceeding of the US National Applied Mechanics*, *1*, 487–491.

Fisher, Q. J., Casey, M., Clennell, M. B., & Knipe, R. J. (1999). Mechanical compaction of deeply buried sandstones of the North Sea. *Marine and Petroleum Geology*, *16*, 605–618. https://doi.org/10.1016/s0264-8172(99)00044-6

Folk, R. L. (1959). Practical petrographic classification of limestones. *AAPG Bulletin*, *43*, 1–38. https://doi.org/10.1306/0BDA5C36-16BD-11D7-8645000102C1865D

Fossum, A. F., & Fredrich, J. T. (2000). Cap plasticity models and dilatant and compactive pre-failure deformation. *Proceedings of the 4th North American Rock Mechanics Symposium*, Seattle, WA, 1169–1176.

Fredrich, J. T., Evans, B., & Wong, T.-f. (1989). Micromechanics of the brittle to plastic transition in Carrara marble. *Journal of Geophysical Research*, *94*, 4129–4145. https://doi.org/10.1029/jb094ib04p04129

Grueschow, E., & Rudnicki, J. W. (2005). Elliptic yield cap constitutive modeling for high porosity sandstone. *International Journal of Solids and Structures*, *42*, 4574–4587. https://doi.org/10.1016/j.ijsolstr.2005.02.001

Hall, S. A., Bornert, M., Desrues, J., Pannier, Y., Lenoir, N., Viggiani, G., & Bésuelle, P. (2010). Discrete and continuum analysis of localised deformation in sand using X-ray μCT and volumetric digital image correlation. *Géotechnique*, *60*, 315–322. https://doi.org/10.1680/geot.2010.60.5.315

Heap, M. J., Baud, P., McBeck, J. A., Renard, F., Carbillet, L., & Hall, S. A. (2020). Imaging strain localisation in porous andesite using digital volume correlation. *Journal of Volcanology and Geothermal Research*, *404*, 107038. https://doi.org/10.1016/j.jvolgeores.2020.107038

Heap, M. J., Kushnir, A. R., Gilg, H. A., Wadsworth, F. B., Reuschlé, T., & Baud, P. (2017). Microstructural and petrophysical properties of the Permo-Triassic sandstones (Buntsandstein) from the Soultz-sous-Forêts geothermal site (France). *Geothermal Energy*, *5*(1), 1–37. https://doi.org/10.1186/s40517-017-0085-9

Heap, M. J., Mollo, S., Vinciguerra, S., Lavallée, Y., Hess, K.-U., Dingwell, D. B., et al. (2013). Thermal weakening of the carbonate basement under Mt. Etna volcano (Italy): Implications for volcano instability. *Journal of Volcanology and Geothermal Research*, *250*, 42–60. https://doi.org/10.1016/j.jvolgeores.2012.10.004

Huang, L., Baud, P., Cordonnier, B., Renard, F., Liu, L., & Wong, T.-f. (2019). Synchrotron X-ray imaging in 4D: Multiscale failure and compaction localization in triaxially compressed porous limestone. *Earth and Planetary Science Letters*, *528*, 115831. https://doi.org/10.1016/j.epsl.2019.115831

ILI. (2007). *Indiana limestone Handbook* (22nd edition). Bedford: Indiana Limestone Institute of America, Inc.

Issen, K. A., & Rudnicki, J. W. (2000). Conditions for compaction bands in porous rock. *Journal of Geophysical Research*, *105*, 21529–21536. https://doi.org/10.1029/2000jb900185

Ji, Y., Baud, P., Vajdova, V., & Wong, T.-f. (2012). Characterization of pore geometry of Indiana limestone in relation to mechanical compaction. *Oil And Gas Science Technology - Rev. IFP Energies nouvelles*, *67*(5), 753–775. https://doi.org/10.2516/ogst/2012051

Ji, Y., Hall, S. A., Baud, P., & Wong, T.-f. (2015). Characterization of pore structure and strain localization in Majella limestone by X-ray computed tomography and digital image correlation. *Geophysical Journal International*, *200*, 701–719. https://doi.org/10.1093/gji/ggu414

Lade, P. V., & Kim, M. K. (1995). Single hardening constitutive model for soil, rock and concrete. *International Journal of Solids and Structures*, *32*, 1963–1978. https://doi.org/10.1016/0020-7683(94)00247-t

Lisabeth, H. P., & Zhu, W. (2015). Effect of temperature and pore fluid on the strength of porous limestone. *Journal of Geophysics Research: Solid Earth*, *120*, 6191–6208. https://doi.org/10.1002/2015JB012152

Louis, L., Wong, T.-f., Baud, P., & Tembe, S. (2006). Imaging strain localization by X-ray computed tomography: Discrete compaction bands in Diemelstadt sandstone. *Journal of Structural Geology*, *28*, 762–775. https://doi.org/10.1016/j.jsg.2006.02.006

Lucia, F. J. (1995). Rock-fabric/petrophysical classification of carbonate pore space for reservoir characterization. *AAPG Bulletin*, *79*, 1275–1300. https://doi.org/10.1306/7834D4A4-1721-11D7-8645000102C1865D

Marinelli, F., & Buscarnera, G. (2015). Parameter calibration for high-porosity sandstones deformed in the compaction banding regime. *International Journal of Rock Mechanics and Mining Sciences*, *78*, 240–252. https://doi.org/10.1016/j.ijrmms.2015.05.004

Meng, F., Baud, P., Ge, H., & Wong, T. f. (2019). The effect of stress on limestone permeability and effective stress behavior of damaged samples. *Journal of Geophysical Research: Solid Earth*, *124*(1), 376–399. https://doi.org/10.1029/2018jb016526

Myer, L. R., Kemeny, J. M., Zheng, Z., Suarez, R., Ewy, R. T., & Cook, N. G. W. (1992). Extensile cracking in porous rock under differential compressive stress. *Applied Mechanics Reviews*, *45*, 263–280. https://doi.org/10.1115/1.3119758

Nicolas, A., Fortin, J., Regnet, J. B., Dimanov, A., & Guéguen, Y. (2016). Brittle and semi-brittle behaviors of a carbonate rock: Influence of water and temperature. *Geophysical Journal International*, *206*, 438–456. https://doi.org/10.1093/gji/ggw154

Rice, J. R. (1975). Continuum mechanics and thermodynamics of plasticity I relation to microscale deformation mechanisms. In A. A. Argon (Ed.), *Constitutive equations in plasticity* (pp. 23–79). MIT Press.

Rudnicki, J. W. (1977). The effect of stress-induced anisotropy on a model of brittle rock failure as localization of deformation. *Proceedings of the 18th US Symposium on Rock Mechanics*, USMRS 1977, Golden, Colorado, 22 June, American Rock Mechanics Association.

Rudnicki, J. W. (2002). Conditions for compaction and shear bands in a transversely isotropic material. *International Journal of Solids and Structures*, *39*(13–14), 3741–3756. https://doi.org/10.1016/s0020-7683(02)00173-7

Rudnicki, J. W. (2004). Shear and compaction band formation on an elliptic yield cap. *Journal of Geophysical Research*, *109*, B03402. https://doi.org/10.1029/2003jb002633

Rudnicki, J. W., & Rice, J. R. (1975). Conditions for the localization of deformation in pressure-sensitive dilatant materials. *Journal of the Mechanics and Physics of Solids*, *23*, 371–394. https://doi.org/10.1016/0022-5096(75)90001-0

Rutter, E. H. (1974). The influence of temperature, strain rate and interstitial water in the experimental deformation of calcite rocks. *Tectonophysics*, *22*, 311–334. https://doi.org/10.1016/0040-1951(74)90089-4

Rutter, E. H. (1986). On the nomenclature of mode of failure transitions in rocks. *Tectonophysics*, *122*, 381–387. https://doi.org/10.1016/0040-1951(86)90153-8

Schubnel, A., Walker, E., Thompson, B. D., Fortin, J., Guéguen, Y., & Young, R. P. (2006). Transient creep, aseismic damage and slow failure in Carrara marble deformed across the brittle-ductile transition. *Geophysical Research Letters*, *33*, L17301. https://doi.org/10.1029/2006GL026619

Stamati, O., Andò, E., Roubin, E., Cailletaud, R., Wiebicke, M., Pinzon, G., et al. (2020). Spam: Software for practical analysis of materials. *Joss*, *5*(51), 2286. https://doi.org/10.21105/joss.02286

Tondi, E., Antonellini, M., Aydin, A., Marchegiani, L., & Cello, G. (2006). The role of deformation bands, stylolites and sheared stylolites in fault development in carbonate grainstones of Majella Mountain, Italy. *Journal of Structural Geology*, *28*, 376–391. https://doi.org/10.1016/j.jsg.2005.12.001

Tondi, E., Rustichelli, A., Cilona, A., Balsamo, F., Storti, F., Napoli, G., et al. (2016). Hydraulic properties of fault zones in porous carbonates, examples from central and southern Italy. *Italian Journal of Geosciences*, *135*, 68–79. https://doi.org/10.3301/ijg.2015.08

Vajdova, V., Baud, P., & Wong, T.-f. (2004). Compaction, dilatancy, and failure in porous carbonate rocks. *Journal of Geophysical Research*, *109*, B05204. https://doi.org/10.1029/2003JB002508

Vajdova, V., Baud, P., Wu, L., & Wong, T.-f. (2012). Micromechanics of inelastic compaction in two allochemical limestones. *Journal of Structural Geology*, *43*, 100–117. https://doi.org/10.1016/j.jsg.2012.07.006

Vajdova, V., Zhu, W., Natalie Chen, T.-M., & Wong, T.-f. (2010). Micromechanics of brittle faulting and cataclastic flow in Tavel limestone. *Journal of Structural Geology*, *32*, 1158–1169. https://doi.org/10.1016/j.jsg.2010.07.007

Wang, Y., Meng, F., Wang, X., Baud, P., & Wong, T.-f. (2018). Effective stress law for the permeability and deformation of four porous limestones. *Journal of Geophysical Research: Solid Earth*, *123*(6), 4707–4729. https://doi.org/10.1029/2018JB015539

Wawersik, W. R., & Fairhurst, C. (1970). A study of brittle rock fracture in laboratory compression experiments. *International Journal of Rock Mechanics and Mining Sciences & Geomechanics Abstracts*, *7*, 561–575. https://doi.org/10.1016/0148-9062(70)90007-0

Wong, T.-f., & Baud, P. (2012). The brittle-ductile transition in porous rock: A review. *Journal of Structural Geology*, *44*, 25–53. https://doi.org/10.1016/j.jsg.2012.07.010

Wong, T.-f., David, C., & Zhu, W. (1997). The transition from brittle faulting to cataclastic flow in porous sandstones: Mechanical deformation. *Journal of Geophysical Research*, *102*, 3009–3025. https://doi.org/10.1029/96jb03281

Yarushina, V., & Podladchikov, Y. (2010). Low-frequency attenuation due to pore-scale inelasticity. *Geophysics*, *75*, 51–63. https://doi.org/10.1190/1.3420734

Zheng, Z., Cook, N. G. W., & Myer, L. R. (1989). Stress induced microcrack geometry at failure in unconfined and confined axial compressive tests. *Proceedings of the U. S. Rock Mechanics Symposium*, *30*, 749–756.

Zhu, W., Baud, P., & Wong, T.-f. (2010). Micromechanics of cataclastic pore collapse in limestone. *Journal of Geophysical Research*, *115*, B04405. https://doi.org/10.1029/2009JB006610